



HAL
open science

Experimental Descriptors for the Synthesis of Multicationic Nickel Perovskite Nanoparticles for Oxygen Reduction

Francisco Gonell, Carlos M Sánchez-Sánchez, Vincent Vivier, Christel Laberty-Robert, David Portehault

► To cite this version:

Francisco Gonell, Carlos M Sánchez-Sánchez, Vincent Vivier, Christel Laberty-Robert, David Portehault. Experimental Descriptors for the Synthesis of Multicationic Nickel Perovskite Nanoparticles for Oxygen Reduction. ACS Applied Nano Materials, 2020, 3 (8), pp.7482-7489. 10.1021/ac-sanm.0c01094 . hal-02912046

HAL Id: hal-02912046

<https://hal.sorbonne-universite.fr/hal-02912046v1>

Submitted on 1 Sep 2020

HAL is a multi-disciplinary open access archive for the deposit and dissemination of scientific research documents, whether they are published or not. The documents may come from teaching and research institutions in France or abroad, or from public or private research centers.

L'archive ouverte pluridisciplinaire **HAL**, est destinée au dépôt et à la diffusion de documents scientifiques de niveau recherche, publiés ou non, émanant des établissements d'enseignement et de recherche français ou étrangers, des laboratoires publics ou privés.

1
2
3
4
5
6
7 Experimental Descriptors for the Synthesis of
8
9
10
11 Multicationic Nickel Perovskite Nanoparticles for
12
13
14
15 Oxygen Reduction
16
17
18
19

20 *Francisco Gonell*^a, *Carlos M. Sánchez-Sánchez*^b, *Vincent Vivier*^b, *Christel Laberty-*
21
22

23
24 *Robert*^a, *David Portehault*^{a, *}
25
26
27

28
29 ^a Sorbonne Université, CNRS, Laboratoire de Chimie de la Matière Condensée de Paris
30
31
32 (CMCP), 4 place Jussieu, F-75005, Paris, France
33
34
35

36
37 ^b Sorbonne Université, CNRS, Laboratoire Interfaces et Systèmes Electrochimiques
38
39
40 (LISE), 4 place Jussieu, F-75005, Paris, France
41
42
43
44
45
46
47
48
49
50
51
52
53
54
55
56
57
58
59
60

1
2
3
4
5
6
7
8
9
10
11
12
13
14
15
16
17
18
19 ABSTRACT
20
21
22
23

24 In many liquid-phase synthesis methods developed to produce nanomaterials, the key
25
26
27 parameters governing the selective synthesis of solids and compounds are clearly
28
29
30 identified, e.g. heat treatment profile, precursors solubility, pH, etc. Most of these well-
31
32
33 understood approaches rely on relatively low temperature processes, below 400 °C,
34
35
36 where conventional solvents are still stable. Interestingly, thermally stable inorganic
37
38 molten salts enable to widen the temperature range for liquid-phase syntheses. They
39
40
41 provide access to other families of crystalline solids requiring higher temperatures, as
42
43
44
45
46
47
48 multicationic oxides. Nonetheless, the mechanisms that govern solid state formation and
49
50
51
52 phase selection when different compounds compete are poorly understood. Herein, we
53
54
55
56 report how experimental parameters, such as temperature, time, reaction medium
57
58
59
60

1
2
3
4 composition and solvent oxo-basicity, enable to drive the synthesis mechanisms in molten
5
6
7 salts towards nanoscaled multicationic oxides. We especially enlighten the phase-
8
9
10 selective synthesis of pseudo-cubic perovskite LaNiO_3 and layered Ruddlesden-Popper
11
12
13 phases La_2NiO_4 and LaSrNiO_4 at the nanoscale, by suggesting that the oxidation state of
14
15
16 the metallic precursor plays a key role in the reaction pathway. This allows designing
17
18
19 electrocatalysts for oxygen reduction reaction.
20
21
22
23
24
25
26
27
28

29 KEYWORDS. perovskite, layered materials, nickel oxide, oxygen reduction reaction,
30
31
32 molten salts, synthesis mechanism.
33
34
35
36
37
38
39
40
41
42
43
44
45
46
47
48
49
50
51
52
53
54
55
56
57
58
59
60

INTRODUCTION

In the last decades, bottom-up nanomaterials synthesis has delivered exciting properties, with a plethora of nanoparticles accessible through solution chemistry, mostly in water or organic solvents. These liquids limit the synthesis temperature up to 350-400 °C. In this temperature range, metallic and ionic solids are easily crystallized. On the opposite, solids bearing a strong covalence character exhibit low crystallinity and even an amorphous character when they are prepared by liquid-phase synthesis. Indeed, such solids require a high temperature to overcome the energy barrier of crystallization, which includes reorganization of directional and strong bonds into the solid. Such high temperatures are energetically costly and trigger large crystal growth, hence inhibiting our ability to synthesize individualized nanoparticles.

This limit can be overcome by performing nanoparticles synthesis in molten salts.¹ These liquid media are especially suited for high temperature syntheses (generally up to 1000 °C),^{1,2} because they are thermally stable, exhibit low vapor pressure and provide liquid media for the synthesis of nanoparticles with an increased reaction rate compared

1
2
3 to solid-state processes. These enhanced kinetics result in a decrease in the grain size.
4
5

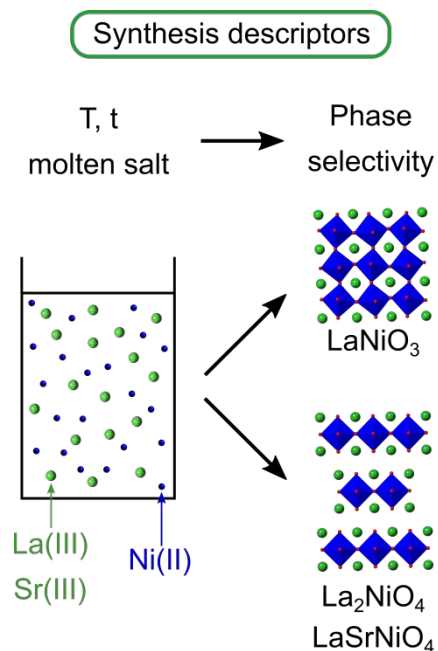
6
7 Molten salts are then ideal to synthesize solids that need harsh conditions to crystallize
8
9
10 through solid-state processes. Other advantages of molten salts encompass their low
11
12
13 cost, low environmental impact and easy implementation at the large scale, as shown by
14
15
16 their current industrial applications.³ Molten salts have delivered materials previously not
17
18
19 available at the nanoscale such as some multicationic oxides,^{4–6} borides,^{7–9} carbides,¹⁰
20
21
22 group VI semiconductors,¹¹ etc. Despite numerous examples showing the rich versatility
23
24
25 of molten salts for synthesis, reports dealing with reaction mechanisms in these media
26
27
28 are scarce. Mechanistic studies would allow better understanding of nanoparticles
29
30
31 formation in molten salts, enable selective synthesis of solids, and further provide design
32
33
34 rules towards nanomaterials with tuned properties.
35
36
37
38
39
40
41
42

43 The perovskite structure can accommodate various anions and cations and shows a high
44
45
46 compositional versatility to address various application fields.^{12–15} This diversity is
47
48
49 reflected into related materials such as Ruddlesden-Popper phases (RPs) with
50
51
52 stoichiometry $A_{n+1}B_nO_{3n+1}$ (or $(AO)(ABO_3)_n$, $n=1, 2, \dots$). RPs are built on $nABO_3$ perovskite
53
54
55
56
57
58
59
60

1
2
3 layers alternating with a AO rock-salt layer. Their transport properties are characteristic
4
5
6
7 of two-dimensional materials.¹⁶ AO layers and oxygen non-stoichiometry provide
8
9
10 additional oxygen ion transport compared to the cubic perovskite structure. Nickel-based
11
12
13 perovskites exhibit structural and compositional versatility, adjustable nickel oxidation
14
15
16 state, ionic and/or electronic conductivity that make these materials widely studied for
17
18
19 spintronics,¹⁷ as redox catalysts in NO_x elimination,¹⁸ and as electrocatalysts of the
20
21 oxygen reduction reaction^{19,20} in cathodes of Li–O₂ batteries^{21,22} and solid oxide fuel
22
23
24 cells.^{23–25}
25
26
27
28
29
30

31
32 Nickel-based perovskites have been produced through solid–state synthesis above
33
34
35 1000 °C, yielding large crystals with uncontrolled morphology.²⁰ Sol-gel pathways have
36
37
38 also been explored to produce materials with smaller crystal size. Yet, the thermal post-
39
40
41 treatment required for crystallization hinders size and morphology control, and delivers
42
43
44 crystals with large amounts of defects that limit charge transport. Molten salts are then
45
46
47 promising media for lowering the synthesis temperature of nickel-based perovskites, to
48
49
50 achieve smaller and more crystallized nanoparticles for tuning catalytic properties.
51
52
53
54
55
56
57
58
59
60

1
2
3
4 In this work, we demonstrate that a careful choice of the synthesis media and reaction
5
6
7 conditions enables the production of LaNiO_3 , La_2NiO_4 and SrLaNiO_4 nanoparticles
8
9
10 through molten salts synthesis (**Scheme 1**). The synthesis mechanisms are studied to
11
12
13 highlight the parameters governing the formation of nanoscaled multicationic oxides with
14
15
16 controlled crystal structure. We then show that controlling the adequate synthesis
17
18
19 parameters enables to tune the electrocatalytic activity of nickel-based perovskites for the
20
21
22 oxygen reduction reaction (ORR) in alkaline solution.
23
24
25
26
27
28



51
52 **Scheme 1.** Schematic representation of selective molten salt syntheses of Ni
53
54
55
56
57
58
59
60 perovskites.

EXPERIMENTAL SECTION

Synthesis. All reagents were purchased from Sigma–Aldrich, otherwise written, and used as received without further purification. The amounts of precursors used in each synthesis are the following: Pseudo–cubic $LaNiO_3$ synthesis: 6.5 mmol of $Ni(NO_3)_2 \cdot 6H_2O$, 6.5 mmol of $La(NO_3)_3 \cdot 6H_2O$, and 65 mmol of KNO_3 or 95 mmol of $NaNO_2$. Layered La_2NiO_4 synthesis: 6.5 mmol of $Ni(NO_3)_2 \cdot 6H_2O$, 13 mmol of $La(NO_3)_3 \cdot 6H_2O$, and 65 mmol of KNO_3 or 95 mmol of $NaNO_2$. Layered $LaSrNiO_4$ synthesis: 6.5 mmol of $Ni(NO_3)_2 \cdot 6H_2O$, 6.5 mmol of $La(NO_3)_3 \cdot 6H_2O$, 6.5 mmol of $Sr(NO_3)_2$ and 95.2 mmol of $NaNO_2$.

For each synthesis, the reagents were mixed with a few drops of ethanol, milled by using a Retsch MM400 ball miller with 50 mL stainless steel bowls filled with one ball. The resulting powder was dried under vacuum at 40 °C overnight. 2.5 g of each mixture was introduced in an alumina crucible and treated in a preheated oven at the corresponding temperature and time discussed in this work. Then, the reaction was quenched at room temperature by removing the crucible from the oven. The resulting black powder was

1
2
3
4 washed by centrifugation with deionized water several times and dried under vacuum at
5
6
7 room temperature overnight.
8
9

10
11 Seeded syntheses were performed to convert previous synthesized particles (seeds) into
12
13 other perovskites: *LaNiO₃*: 0.25 g of La_2NiO_4 , 0.6 mmol of $\text{Ni}(\text{NO}_3)_2 \cdot 6\text{H}_2\text{O}$ and 2.5 g of
14
15 NaNO_2 were milled in an agate mortar and dried overnight at 40 °C under vacuum. This
16
17
18 mixture was introduced in an alumina crucible and treated at several temperatures and
19
20
21 times. *La₂NiO₄*: 0.25 g of LaNiO_3 , 0.1 mmol of $\text{La}(\text{NO}_3)_3 \cdot 6\text{H}_2\text{O}$ and 2.5 g of NaNO_2 were
22
23
24 milled in an agate mortar and dried overnight at 40 °C under vacuum. This mixture was
25
26
27 introduced in an alumina crucible and treated at 800 °C for 0.5 hours. *LaSrNiO₄*: 0.25 g
28
29
30 of LaNiO_3 or 0.41 g of La_2NiO_4 , 0.1 mmol of $\text{Sr}(\text{NO}_3)_2$ and 2.5 g of NaNO_2 were milled in
31
32
33 an agate mortar and dried overnight at 40 °C under vacuum. This mixture was introduced
34
35
36 in an alumina crucible and treated at 800 °C. After 1 hour, all reaction media were
37
38
39 quenched at room temperature, washed with deionized water several times and dried at
40
41
42 room temperature under vacuum overnight.
43
44
45
46
47
48
49
50
51
52
53
54
55
56
57
58
59
60

1
2
3
4 Stability tests of the preformed materials in the reaction media, so-called “blank
5
6
7 experiments” were performed with 0.25 g of the previously synthesized material, which
8
9
10 was mixed with 2.5 g of NaNO_2 and milled in an agate mortar, then dried overnight at
11
12
13
14 40 °C under vacuum. This mixture was introduced in an alumina crucible and treated at
15
16
17 the same temperature and time required for obtaining the targeted material (optimal
18
19
20 conditions previously studied). Then, the synthesis media was quenched at room
21
22
23
24 temperature and the as-synthesized material was washed with deionized water several
25
26
27
28 times and dried at room temperature under vacuum overnight.
29
30

31
32 **Characterization.** Powder X-ray Diffraction (XRD) was performed on a Bruker D8
33
34
35
36 advance diffractometer equipped with a Cu $K\alpha$ source. High resolution transmission
37
38
39 electron microscopy (HRTEM) was carried out on a JEOL JEM2100Plus LaB_6 working at
40
41
42
43 an accelerating voltage of 200 kV and field-emission scanning electron microscopy
44
45
46 (SEM) on a Hitachi SU-70 microscope. XRD and electron diffraction patterns were
47
48
49
50 indexed along the 00-033-0711, 00-034-0314, 04-007-0158 references from the PDF-4
51
52
53
54 database for LaNiO_3 , La_2NiO_4 , LaSrNiO_4 , respectively. The atomic composition was
55
56
57
58
59
60

1
2
3 measured by inductively coupled plasma optical emission spectrometry (ICP–OES) on a
4
5
6
7 Varian Vista analyzer. The surface area was calculated from the adsorption branch of the
8
9
10 N₂ sorption isotherm according to the BET method at 77 K using an ASAP 2010
11
12
13
14 equipment. Prior to sorption measurements, the powders were degassed at 300 °C for
15
16
17 4h.
18
19
20
21

22 The electrocatalytic properties were studied through a three-electrode setup, using a
23
24
25 rotating disk electrode (RDE) made of glassy carbon as working electrode, a Pt wire as a
26
27
28 counter electrode and an Ag/AgCl electrode as reference connected to a VPS Biologic
29
30
31 potentiostat. As previously described,²⁶ a conductive ink containing the electrocatalyst
32
33
34
35
36 (10 mg), black carbon (10 mg) and Nafion (435 μL) in ethanol (10 mL) was deposited on
37
38
39 the polished glassy carbon (0.07 cm²) of the RDE after sonification for 1 hour and then
40
41
42 dried for 1 hour. 10 μL were deposited for performing cyclic voltammetry (CV) and lower
43
44
45 amounts (2 μL) of the ink were used in order to see the catalyst deactivation during
46
47
48
49 chronopotentiometry (current density: 0.5 mA cm⁻²_{disk}). For comparison with benchmark
50
51
52
53 catalys a ink with 20 % Pt/C (Alfa Aesar) was prepared using 12.5 mg of the material and
54
55
56
57
58
59
60

1
2
3 the same amounts of EtOH and Nafion-117 as before. 1.5 μL of this ink was deposited
4
5
6
7 on the GC electrode for performing the CV. The films were hydrated with one drop of
8
9
10 0.1 M KOH electrolyte during 30 min before the experiments. All the measurements were
11
12
13 performed in O_2 -saturated electrolyte at a 10 mV s^{-1} scan rate and a rotation rate of
14
15
16
17 1600 rpm. Each experiment was repeated 3 times to ensure reproducibility. Especially,
18
19
20 the Koutecky-Levich analysis was performed for each sample on three different
21
22
23 electrodes. The number of electrons exchanged was evaluated by averaging the two CV
24
25
26
27 branches for each measurement. The numbers of electrons calculated for three different
28
29
30 electrodes were then averaged and the different measurements enabled to evaluate the
31
32
33 uncertainty at ± 0.2 for each sample.
34
35
36
37
38

39 RESULTS AND DISCUSSION

40
41
42
43

44 The synthesis of LaNiO_3 and La_2NiO_4 was performed using metal nitrates (La(III) and
45
46
47 Ni(II)) of varying ratios. KNO_3 was used as solvent to dissolve metal nitrates and to
48
49
50 efficiently supply oxygen for the synthesis of perovskites.^{4,27} The powder X-ray diffraction
51
52
53 (XRD) patterns for the LaNiO_3 system (**Figure S1**) indicate that high temperature (800 $^\circ\text{C}$)
54
55
56
57
58
59
60

1
2
3 treatments and long reaction times (6 hours) are needed to obtain pure LaNiO_3 . When
4
5
6
7 the ratio of La and Ni reagents is adjusted to target La_2NiO_4 , even prolonged heating at
8
9
10 $800\text{ }^\circ\text{C}$ for 14 h yields LaNiO_3 as the major product with a small amount of La_2NiO_4 (**Figure**
11
12
13
14 **S2**). The results suggest that in KNO_3 , the reagents are not sufficiently reactive to yield
15
16
17 LaNiO_3 below $800\text{ }^\circ\text{C}$ and to form single-phase La_2NiO_4 . We then investigated a solvent
18
19
20 prone to increase the reactivity of the initial metal salts by acting as a better O^{2-} source.
21
22
23
24
25 NaNO_2 is a good candidate thanks to its high oxo-basicity.²⁸ NaNO_2 has been efficiently
26
27
28 used as synthesis medium for several systems including ZrO_2 ,^{28–30} MgO ,³¹
29
30
31 $\text{La}_{0.5}\text{Sr}_{1.5}\text{MnO}_4$.²⁶ Indeed, the reactivity of Ni(II) and La(III) nitrates drastically increases in
32
33
34
35 NaNO_2 (**Figure 1a**). NaNO_2 yields a mixture of LaNiO_3 and La_2NiO_4 at $600\text{ }^\circ\text{C}$ (**Figure 1a**),
36
37
38 while LaNiO_3 could not be detected in KNO_3 in similar conditions (**Figure S1**). The
39
40
41 proportion of LaNiO_3 increases with the reaction time, as shown by the increased relative
42
43
44 intensity of the corresponding XRD peaks. Minor amounts of NiO are also detected at
45
46
47
48
49 $600\text{ }^\circ\text{C}$ (**Figure 1a**). The crystal size calculated from XRD for LaNiO_3 obtained at
50
51
52
53
54
55
56
57
58
59
60

1
2
3
4 600 °C/8 h is 33 nm and the surface area is 9 m² g⁻¹ according to N₂ sorption. Inductively
5
6
7 coupled plasma (ICP) analysis confirmed the expected La:Ni ratio 1:1.
8
9

10
11 Scanning (SEM) and transmission (TEM) electron microscopies show that LaNiO₃ is
12
13
14 composed of well faceted truncated cubes with an average size of 100 nm (**Figure 1b–d**).
15
16

17
18 Smaller 20 nm particles are also visible in these images. Energy dispersive X-ray (EDX)
19
20
21 analysis indicates only the presence of Ni and O in these particles, in agreement with high
22
23

24
25 resolution TEM (HRTEM, **Figure S3**) indicating the NiO structure, as powder XRD
26
27

28
29 (**Figure 1a**). Focusing on the 100 nm particles (**Figure 1e**), the selected area electron
30
31

32
33 diffraction (SAED) pattern can be indexed over LaNiO₃ structure. Interestingly, seemingly
34
35

36
37 aggregated particles show a single crystal-like pattern, indicating highly oriented crystals.
38

39
40 **Figure 1f** shows a HRTEM micrograph of a particle
41
42
43
44
45
46
47
48
49
50
51
52
53
54
55
56
57
58
59
60

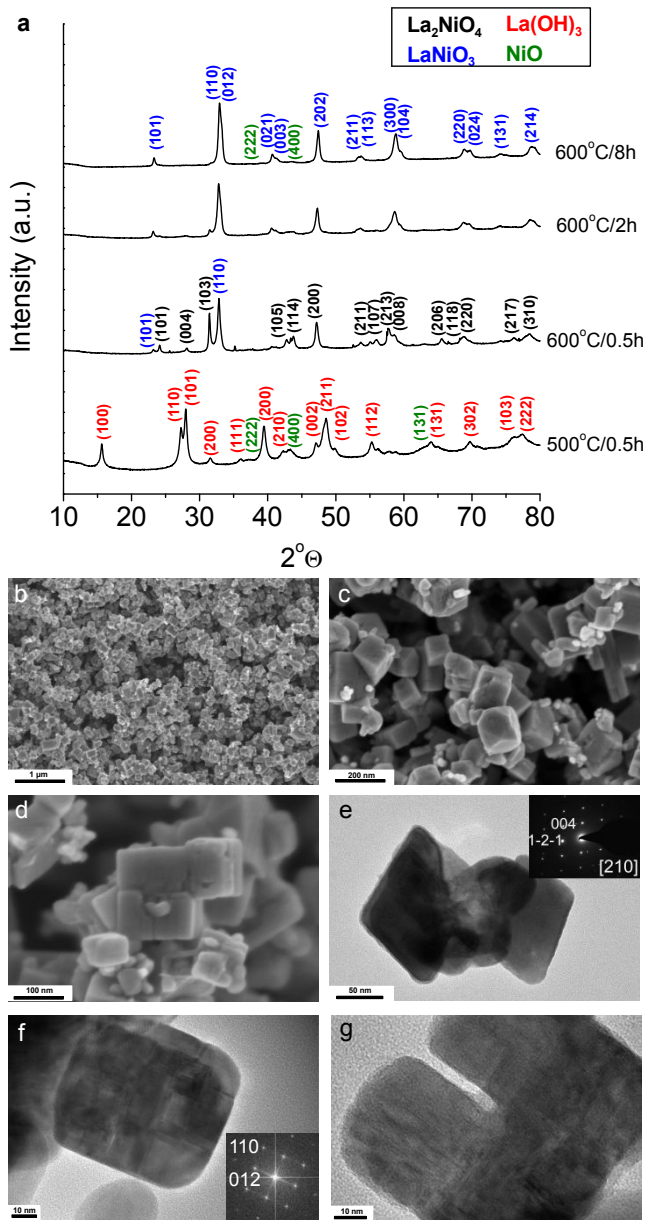


Figure 1. (a) XRD diagrams of the powders obtained at different temperatures and reaction times when targeting LaNiO_3 in NaNO_2 . Electron microscopy study of LaNiO_3 (600 °C/8h): (b–d) SEM and (e) TEM images (inset shows the corresponding SAED

1
2
3
4 pattern of the particles ensemble. (f, g) HRTEM image (inset shows the corresponding
5
6
7 FFT). The SAED and FFT are indexed along the LaNiO_3 structure.
8
9

10
11 of 80 nm diameter, which can again be fully indexed on the LaNiO_3 structure. The material
12
13
14 is then composed of a majority of ~ 100 nm LaNiO_3 cubes with small amounts of 20 nm
15
16
17
18 NiO particles. The LaNiO_3 particle size measured by electron microscopy is larger than
19
20
21 the one calculated by XRD. This discrepancy might originate from the ~ 100 nm particles
22
23
24
25 **(Figure 1d and 1g)** being formed by aggregation of smaller cubic particles. ~ 30 nm cubic
26
27
28 particles are indeed perfectly oriented in respect to each other within large cubes. The
29
30
31 defects at the grain boundaries may limit the lattice coherence, yielding small XRD crystal
32
33
34
35 size, even if the primary grains are iso-oriented as shown by SAED and HRTEM.
36
37
38
39

40 When the La:Ni ratio is increased in order to obtain the RP phase La_2NiO_4 , the behavior
41
42
43 of the reaction medium changes completely. At 600°C , the product is a mixture of
44
45
46
47 $\text{La}(\text{OH})_3$ and La_2NiO_4 **(Figure 2a)**. The content of the RP phase increases with the
48
49
50 temperature up to 800°C . When the reaction time is increased from 0.5 h to 2 h, the
51
52
53
54 layered phase disappears at the benefit of hydroxides. Then, in the optimal
55
56
57
58
59
60

1
2
3
4 temperature/time conditions (800 °C/0.5 h), the La:Ni ratio was adjusted by decreasing
5
6
7 the La concentration and keeping constant the Ni content, in order to avoid the formation
8
9
10 of La(OH)₃ impurity. For the nominal ratio La:Ni = 1.8:1, the La(OH)₃ content is minimized
11
12
13
14 (**Figure S4**). The material then consists in La₂NiO₄ with minor amounts of lanthanum
15
16
17 hydroxide. The La₂NiO₄ crystal size calculated from XRD patterns is 76 nm and the
18
19
20 surface area evaluated by N₂ adsorption is 9 m² g⁻¹. The composition evaluated by ICP
21
22
23 analysis matches La₂NiO₄. SEM and TEM indicate that La₂NiO₄ is composed of faceted
24
25
26
27 60 nm nanoparticles (**Figure 2b–e**), in agreement with the Scherrer crystallite size. SAED
28
29
30 shows that the material is composed by single crystal nanoparticles randomly oriented
31
32
33
34 (**Figure 2c**). Some grain boundaries can also be observed, showing iso-oriented crystals
35
36
37
38 (**Figure 2d and e**).

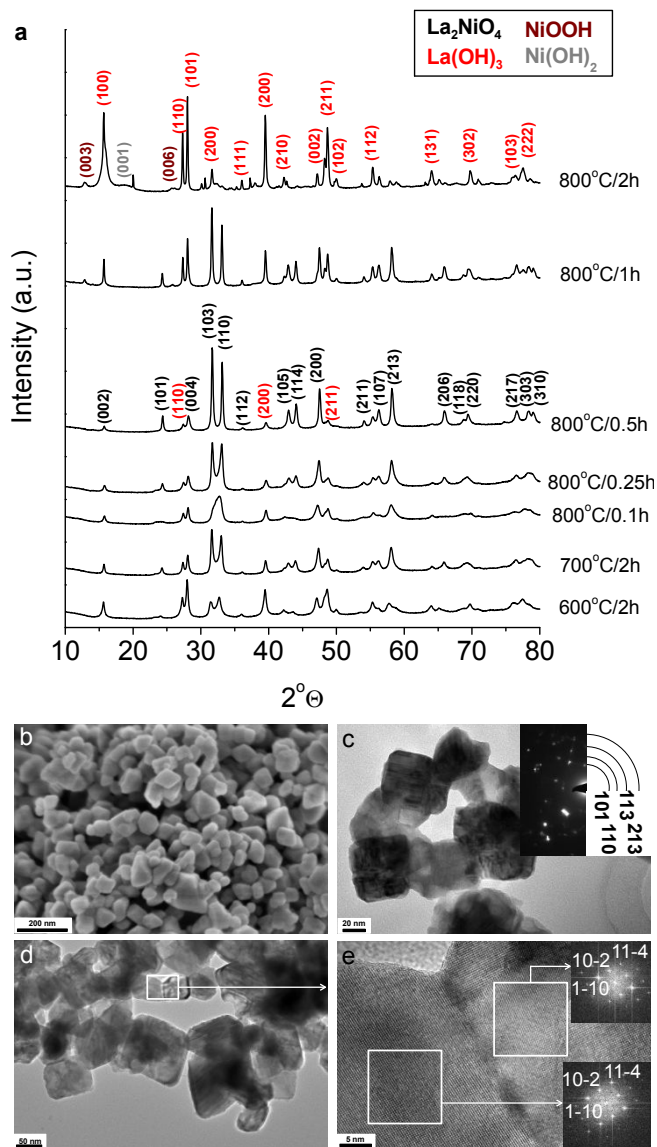


Figure 2. (a) XRD diagrams of the powders obtained at different temperatures and reaction times when targeting La_2NiO_4 in NaNO_2 . Electron microscopy images of La_2NiO_4 (800 °C/0.5h) (b) SEM and (c and d) low magnification TEM images (inset in c shows the corresponding SAED pattern indexed along the La_2NiO_4 structure). (e) HRTEM image

1
2
3 (insets shows the corresponding FFTs of each area in the squares. They are indexed
4
5
6
7 along the La_2NiO_4 structure).
8
9

10
11 Compared to KNO_3 , the use of NaNO_2 as solvent enables a 200 °C decrease of the
12
13
14 reaction temperature for obtaining the pseudo-cubic perovskite. On the other side, the
15
16
17 selectivity towards the layered perovskite structure drastically increases, so that the
18
19
20 pseudo-cubic phase could not be detected in the whole synthesis temperature range. The
21
22
23 higher Lux-Flood basicity that NO_2^- shows compared to NO_3^- indicates its larger
24
25
26 propensity to deliver O^{2-} in the synthesis media.²⁸ Indeed the dissociation constant to
27
28
29 oxide anions is 10^{10} higher for nitrites than for nitrates.²⁸ The increase in the O^{2-}
30
31
32 concentration, namely the oxo-basicity, may equalize cations reactivity, as it is reported
33
34
35 in aqueous media with Brønsted basicity at high pH.³² Such a behavior is also well
36
37
38 documented in non-hydrolytic sol-gel synthesis of titanate perovskites,³³ which results
39
40
41 from the reactivity of the different cations being very similar in e.g. benzylic alcohol.³³
42
43
44 Hence, the increase in oxo-basicity should result in the common incorporation of different
45
46
47 cations in the same compound. The higher oxo-basicity of molten nitrites also drives
48
49
50
51
52
53
54
55
56
57
58
59
60

1
2
3 phase selectivity to oxygen-rich solids, hence favoring the RP phase versus the pseudo-
4
5
6
7 cubic perovskite.
8
9

10
11 The high versatility of molten salt syntheses allowed expanding the range of layered
12
13 perovskites by replacing lanthanum with strontium. **Figure 3a** shows the evolution of the
14
15 crystalline structure as a function of the synthesis temperature and time towards
16
17 LaSrNiO₄. At 600 °C, the XRD peaks can be assigned to La₂NiO₄, which is confirmed by
18
19 EDX that does not detect Sr. By increasing the temperature, Sr could be incorporated in
20
21 the material (La₂NiO₄ and Sr₄Ni₃O₉ at 700 °C). At 800 °C and 0.5 h, the peaks
22
23 corresponding to (103) and (110) planes of the layered perovskite structure show a
24
25 shoulder, which indicates the presence of La₂NiO₄ and LaSrNiO₄. After 1 h at 800 °C,
26
27
28
29
30
31
32
33
34
35
36
37
38
39
40
41
42
43
44
45
46
47
48
49
50
51
52
53
54
55
56
57
58
59
60
La₂NiO₄ disappears and LaSrNiO₄ remains the major product. The XRD crystal size of
LaSrNiO₄ is 49 nm, with a BET surface area of 13 m² g⁻¹ and a well faceted

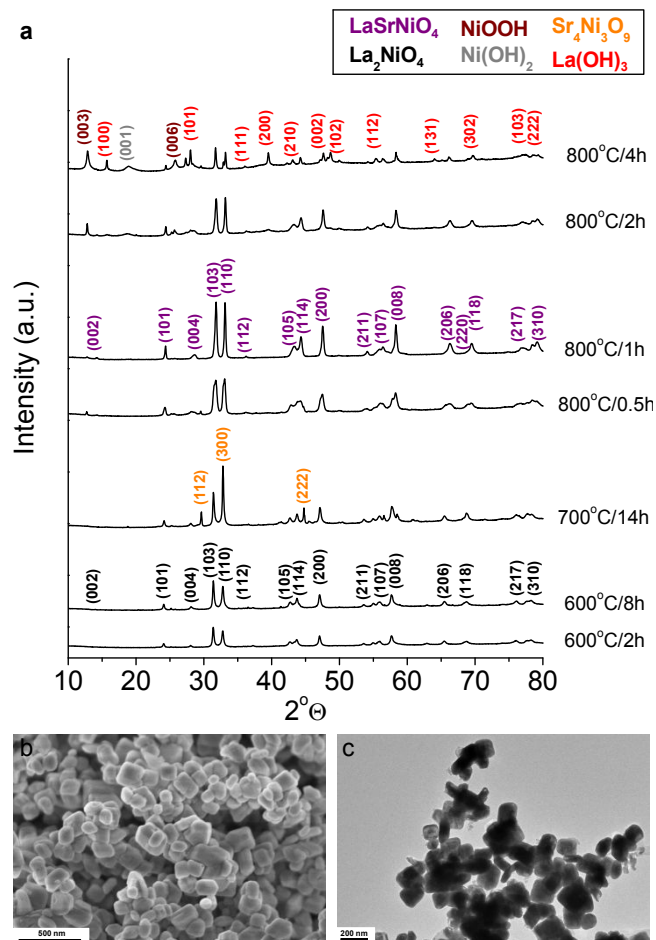


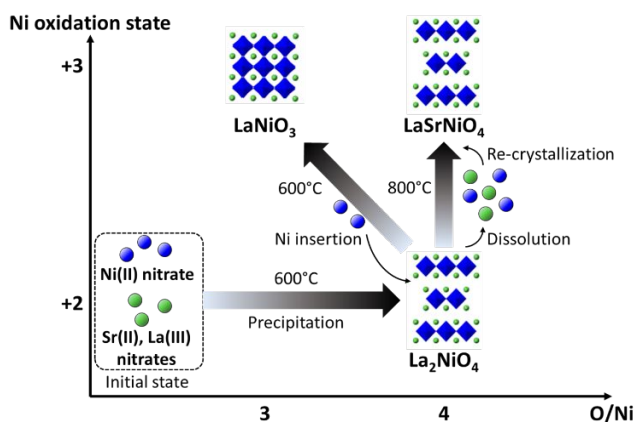
Figure 3. (a) XRD diagrams of the powders obtained at different temperatures and reaction times when targeting LaSrNiO_4 in NaNO_2 . (b) SEM and (c) TEM micrographs of LaSrNiO_4 obtained at $800^\circ\text{C}/1\text{h}$.

morphology of platelets of 100–200 nm basal face and 50 nm thickness (**Figure 3b** and **c**). If the synthesis time is prolonged beyond 1 h, the XRD peaks of the layered compound disappear, showing that the RP phase decomposes. The final product obtained after

1
2
3 washing is composed of several single cation hydroxides. No significant change in the
4
5
6
7 XRD patterns (**Figure S5**), morphology (**Figure S6a and b**) and composition (**Table S1**)
8
9
10 was observed when the content of strontium in the reaction medium was increased. When
11
12
13
14 no strontium was introduced, the product was a mixture of different single cation
15
16
17 (oxy)hydroxides. This observation highlights the importance of strontium to stabilize the
18
19
20 Ruddlesden-Popper structure, in good agreement with the decomposition of La_2NiO_4 at
21
22
23
24 $800\text{ }^\circ\text{C}/1\text{h}$ (**Figure 3a**). A slight shift of (103) and (110) planes towards lower angles is
25
26
27 observed when the Sr content decreases, in agreement with the decreasing amount of
28
29
30 strontium in the materials (**Table S1**) and the expected increase of the lattice parameters
31
32
33
34 in relation with the ionic radii of La(III) (1.15 \AA) and Sr(II) (1.13 \AA). The material with the
35
36
37 lowest strontium content (La:Ni:Sr 1:1:0.2) shows particle a size around 70 nm very
38
39
40 similar that the one when targeting La_2NiO_4 (**Figure S6c and d**).
41
42
43
44
45

46 A common feature is observed for the pathways of crystallization in all the syntheses
47
48
49 reported above. In the two systems LaNiO_3 and LaSrNiO_4 , low temperatures and short
50
51
52 reaction times result La_2NiO_4 as an intermediate product. Such behavior can be explained
53
54
55
56
57
58
59
60

on the basis of nickel oxidation state (OS). The nickel precursor used in the synthesis is nickel(II) species, as in the intermediate phase La_2NiO_4 . Hence, the two different reaction media evolve through a first step involving no redox processes, but only the basicity of the solvent: the first step consists in the evolution through constant oxidation state Ni(II). Then, in a second step, nickel appears to be oxidized to Ni(III) and yield LaNiO_3 and LaSrNiO_4 , depending on the medium composition. Hence, we suggest that the nickel oxidation state drives phase selectivity during the synthesis (**Scheme 1**).



Scheme 2. Proposed mechanisms involved in the synthesis of nickel-based perovskites.

If the nickel oxidation state drives the crystallization pathways of nickel-based perovskites in NaNO_2 , the mechanisms of transformation from the intermediate phase La_2NiO_4 to the

1
2
3 final compounds in molten NaNO_2 require further discussion. In order to shed light on this
4
5
6
7 aspect, syntheses have been performed by using preformed perovskite particles in the
8
9
10 presence (seeded synthesis) and in the absence (blank synthesis) of the metal salt
11
12
13
14 precursor required to reach the adequate stoichiometry in the final product.
15
16
17

18 Treating La_2NiO_4 in molten NaNO_2 without metal salt, the structure is stable in that solvent
19
20
21 at 600 °C for 8 h, the conditions of formation of LaNiO_3 (**Figures 1 and S17a**). The particle
22
23
24 size however increases to 100 nm (**Figure S8**), which is probably caused by severe heat-
25
26
27 treatment conditions. When the stoichiometric amount of $\text{Ni}(\text{NO}_3)_2 \cdot 6\text{H}_2\text{O}$ is introduced in
28
29
30 order to reach LaNiO_3 , the phase evolution observed (**Figure S7b and c**) is similar to the
31
32
33 direct synthesis of LaNiO_3 from the metal salts. When the temperature of synthesis is
34
35
36 raised to 800 °C, the perovskite structure decomposes, yielding (oxy)hydroxides (**Figure**
37
38
39
40
41
42
43 **S7d**). These species are observed after washing the NaNO_2 salt with water. They most
44
45
46 probably indicate dissolution of the perovskite into molten NaNO_2 .³⁴ TEM micrographs
47
48
49
50 (**Figure S9, S10 and S11**) of the intermediate sample formed from the La_2NiO_4 seeds
51
52
53 (600 °C/1h) show particles of 100–200 nm surrounded by nanoparticles of 50 nm, and
54
55
56
57
58
59
60

1
2
3 smaller nanoparticles of 5 nm. The elemental distribution of this intermediate state was
4
5
6
7 mapped by Scanning TEM coupled to Energy Dispersive X-ray Spectroscopy
8
9
10 (STEM-EDS, **Figures S10** and **S11**). The 100–200 nm and 50 nm cubes are composed
11
12
13 by La, Ni and O homogeneously distributed, while smaller 5 nm particles are made of Ni
14
15
16 and O. HRTEM (**Figure S12**) shows that the crystal lattice of the 100-200 nm cubic
17
18
19 particles corresponds to the LaNiO_3 structure, in agreement with the collocation of La, Ni
20
21
22 and O. The 50 nm particles show lattice fringes in agreement with the La_2NiO_4 structure
23
24
25 (**Figure S13**), while the ~5 nm particles at the surface of the larger ones are amorphous
26
27
28 and composed by Ni and O. Finally, the sample obtained after 8 h at 600 °C (**Figure S14**)
29
30
31 shows the same 100 nm well faceted cubic morphology as in the original synthesis from
32
33
34 the La(III) and Ni(II) salts.
35
36
37
38
39
40
41
42

43 The stability of La_2NiO_4 particles in molten NaNO_2 in the conditions of formation of LaNiO_3
44
45
46 (temperature, time), and their morphological, structural and compositional evolution when
47
48
49 reacted with nickel (II) nitrate suggest that the formation of LaNiO_3 goes through insertion
50
51
52 of the dissolved nickel(II) species into the layered RP La_2NiO_4 structure (**Scheme 1**). This
53
54
55
56
57
58
59
60

1
2
3 cation insertion may occur through a topochemical transformation, as observed for
4
5
6
7 several layered perovskites.⁵ A hint of such a reaction mechanism may be found in the
8
9
10 persistence of the morphology of the La_2NiO_4 particles in the final product. In the present
11
12
13 case, the LaNiO_3 product from the seeded synthesis is obtained as particles of c.a. 100
14
15
16 nm. During the transformation, one can distinguish smaller building blocks (**Figure S12**)
17
18
19 also observed in the direct synthesis from the metal salts (**Figure 1g**). These blocks may
20
21
22 be originally the ca. 50 nm La_2NiO_4 nanoparticles that have reacted and coalesced.
23
24
25
26
27
28

29 Blank and seeded syntheses from LaNiO_3 and La_2NiO_4 particles in the same conditions
30
31
32 of synthesis of La_2NiO_4 and LaSrNiO_4 , respectively, yield mixtures of (oxy)hydroxides
33
34
35 after washing (**Figure S15** and **S16**). Therefore, the precursor particles were decomposed
36
37
38 and the cations were dissolved in the reaction medium. This observation suggests that
39
40
41 the synthesis goes through a dissolution-reprecipitation mechanism (**Scheme 1**).³² The
42
43
44 difference in the synthesis mechanism toward LaNiO_3 on one side, La_2NiO_4 and LaSrNiO_4
45
46
47 on the other side, going through topochemical transformation and dissolution-
48
49
50 reprecipitation, respectively, can be explained in terms of synthesis temperatures. Indeed,
51
52
53
54
55
56
57
58
59
60

1
2
3 it is possible to hypothesize that at 600 °C, the temperature may not be sufficient to trigger
4
5
6
7 dissolution of intermediate La_2NiO_4 , so that its transformation to pseudo-cubic LaNiO_3
8
9
10 occurs within the La_2NiO_4 particles. At higher temperature, 800 °C, the dissolution of
11
12
13 intermediate phases is increased and enables crystallization by dissolution followed by
14
15
16
17 re-precipitation (**Scheme 1**).
18
19

20
21
22 The diversity of nanostructured ligand-free nickel-based perovskites, with lack of defects,
23
24
25 obtained through molten salts synthesis provides a unique opportunity to study the
26
27
28 influence of the crystal structure of perovskite-related oxides in the oxygen reduction
29
30
31 reaction (ORR). In order to study these properties, a conductive ink was prepared with
32
33
34
35
36 each catalyst and deposited on a rotating disk electrode (RDE), as described in the
37
38
39 experimental section. The cyclic voltammograms (CVs) were recorded using a three
40
41
42 electrode setup, at a rotating speed of 1600 rpm, in O_2 saturated 0.1M KOH. Note that
43
44
45
46 the possible impurities detected by XRD (lanthanum hydroxide, nickel oxide) are not
47
48
49 active³⁵ in ORR so that the electrocatalytic activities measured originate from the
50
51
52 perovskite materials.
53
54
55
56
57
58
59
60

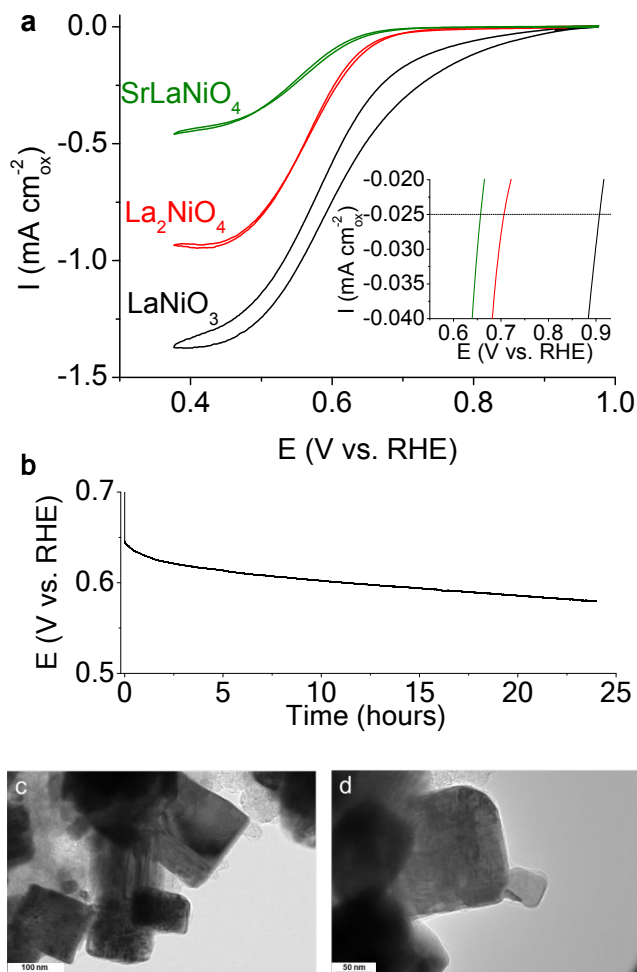


Figure 4. (a) Cyclic voltammograms in ORR conditions (oxide surface-normalized specific activity, O₂-saturated 0.1 M KOH electrolyte) of (a) LaNiO₃, La₂NiO₄ and SrLaNiO₄ at 1600 rpm. The inset shows a zoom of the onset region. (b) Chronopotentiometry curve of LaNiO₃ at 0.5 mA cm⁻²_{disk}, (c and d) TEM images of LaNiO₃ after chronopotentiometry. The light contrast particles of 50 nm in (c) are carbon black particles used as conductive additive.

1
2
3
4 The oxide surface area-normalized cyclic voltammograms (CVs) (**Figure 4a, Figure S17**)
5
6
7 show that LaNiO_3 is the most active material followed by La_2NiO_4 and SrLaNiO_4 with a
8
9
10 potential at $25 \mu\text{A cm}^{-2}_{\text{ox}}$ of 0.91, 0.71 and 0.66 V/RHE, respectively. Tafel slopes
11
12
13 (**Figure S18**) are 56, 208 and 152 $\text{mV}\cdot\text{dec}^{-1}$ for LaNiO_3 , La_2NiO_4 and LaSrNiO_4
14
15
16 respectively, in good agreement with previous works³⁶ and with the overpotentials
17
18
19 described above, where the most active materials show lower slopes. The values
20
21
22 obtained for LaNiO_3 are in agreement with the values previously reported on bulk
23
24
25 materials,^{19,37} thus highlighting the high crystallinity of the nanoparticles. Noteworthy,
26
27
28 crystallization and significant electrocatalytic activity are triggered by syntheses in molten
29
30
31 salts at lower temperature than by using sol-gel and solid-state derived methodologies.
32
33
34
35
36
37
38 LaNiO_3 shows a half-wave potential of 0.61 V vs RHE. This value is lower than for the
39
40
41 benchmark Pt/C electrocatalyst (**Figure S19**) but is comparable to other active
42
43
44 perovskites.³⁸ As other perovskite electrocatalysts, the nickelates reported herein have
45
46
47
48 the advantage of not containing any precious metal.
49
50
51
52
53
54
55
56
57
58
59
60

1
2
3
4 The order of activity $\text{LaNiO}_3 > \text{La}_2\text{NiO}_4 > \text{SrLaNiO}_4$ can be explained by the filling of the
5
6
7 Ni 3d orbitals.¹⁹ According to Shao- Horn *et al.*¹⁹ perovskites bearing B-site transition
8
9
10 metals with configurations d^4 or d^7 show the highest ORR activity because e_g degenerated
11
12
13 orbitals hold one electron for optimal O_2 adsorption.¹⁹ The d^7 configuration of nickel in
14
15
16 $\text{LaNi}^{\text{III}}\text{O}_3$ then explains its highest activity. On the contrary, La_2NiO_4 exhibits a d^8
17
18
19 configuration with lower activity. $\text{SrLaNi}^{\text{III}}\text{O}_4$ seems to deviate from the d^4/d^7 rule as it
20
21
22 shows the lowest activity despite a d^7 configuration. Surface termination with Sr^{2+} and
23
24
25 La^{3+} cations instead of catalytically active nickel may explain this discrepancy. The
26
27
28 number of electrons involved in the ORR according to the Koutecky-Levich analysis
29
30
31 (Figures S20, S21 and S22) is 3.5, 3.4 and 3.0 (± 0.2) electrons per O_2 for LaNiO_3 ,
32
33
34 La_2NiO_4 and SrLaNiO_4 respectively, suggesting a mixture of 4- and 2- electron
35
36
37 mechanisms. The stability of LaNiO_3 during ORR was studied with chronopotentiometry
38
39
40 (Figure 4b), showing only a slight deactivation during 24 hours operation. The potential
41
42
43 required for reaching a current density of $0.5 \text{ mA cm}^{-2}_{\text{disk}}$ evolves from -0.65 to -
44
45
46 0.58 V/RHE. This is reflected in the downward shift of the CVs from the initial state to the
47
48
49 final state (Figure S23). This slight decay may arise from the partial reduction of Ni(III) to
50
51
52
53
54
55
56
57
58
59
60

1
2
3 less active Ni(II) under the reductive conditions applied during the stability test. HRTEM
4
5
6
7 **(Figure 4c-d)** shows no significant change of the well faceted cubic morphology after
8
9
10 chronopotentiometry. In addition, STEM-EDS mapping for LaNiO_3 after
11
12
13
14 chronopotentiometry shows homogeneous Ni and La distribution **(Figure S24)**, while the
15
16
17 atomic composition remains constant, according to EDS analysis. These data further
18
19
20 support the stability of the LaNiO_3 particles under operation thanks to their high
21
22
23
24 crystallinity.
25
26
27
28
29
30
31
32

33 CONCLUSION

34
35
36
37
38 In this work an accurate choice of the synthetic conditions (temperature, time and solvent
39
40
41 oxo-basicity) in molten salts led to the selective synthesis of LaNiO_3 , La_2NiO_4 and
42
43
44
45 LaSrNiO_4 as new nanomaterials that are active electrocatalysts of the oxygen reduction
46
47
48 reaction in alkaline media. Reaction intermediates were identified to shed light on the key
49
50
51 parameters controlling the formation of nickel-based perovskites in molten salts. Nickel
52
53
54
55 oxidation state governs the perovskite formation, through a common low oxidation state
56
57
58
59
60

1
2
3 Ni(II) intermediate (La_2NiO_4) formed from a Ni(II) salt precursor. The intermediate La_2NiO_4
4
5
6
7 phase then evolves to structures with higher Ni oxidation state depending on the
8
9
10 composition of the reaction medium and on the temperature. Low temperatures (600 °C)
11
12
13 favor a topochemical transformation where nickel species in solution are inserted into the
14
15
16 reaction intermediate La_2NiO_4 . At higher temperature, the energy input is high enough to
17
18
19 trigger dissolution of the precursors promoting a dissolution-reprecipitation pathway.
20
21
22
23
24

25 These results highlight experimental descriptors that govern the formation of
26
27
28 nanoparticles of multicationic oxides in molten salts media. We suggest that the oxidation
29
30
31 state of the precursor determines the nature of the reaction intermediate, whose further
32
33
34 evolution is driven by the composition of the medium and the temperature. These reaction
35
36
37 rules should enable further design of synthesis protocols towards multicationic oxides at
38
39
40 nanoscale and electrocatalysts for the oxygen reduction reaction and the oxygen
41
42
43 evolution reaction.
44
45
46
47
48
49
50
51
52
53
54

55 ASSOCIATED CONTENT
56
57
58
59
60

1
2
3 **Supporting Information.**
4
5
6
7

8 The Supporting Information is available free of charge at
9

10
11 <https://pubs.acs.org/doi/xxxxxxxxxxxxx>
12
13

14
15
16 Additional XRD, TEM, electrocatalytic and ICP characterization (PDF).
17
18
19
20
21
22

23
24 **AUTHOR INFORMATION**
25
26
27

28 **Corresponding Author**
29
30

31 *E-mail: david.portehault@sorbonne-universite.fr
32
33
34
35

36 **Funding Sources**
37
38
39

40 The whole research program received financial support from Region Ile-de-France in
41
42
43 the framework of the Domaine d'Intérêt Majeur DIM Nano-K and from the French
44
45
46 national agency for research (ANR) with the project SALTYSPIIN ANR-17-CE09-0005.
47
48
49
50 DP and FG also acknowledge support from the Fondation Collège de France.
51
52
53

54 **Notes**
55
56
57
58
59
60

1
2
3
4 The authors declare no competing financial interest.
5
6
7
8
9
10

11 REFERENCES
12
13
14

- 15 (1) Liu, X.; Fechler, N.; Antonietti, M. Salt Melt Synthesis of Ceramics, Semiconductors
16
17
18 and Carbon Nanostructures. *Chem. Soc. Rev.* **2013**, *42* (21), 8237–8265.
19
20
21 <https://doi.org/10.1039/c3cs60159e>.
22
23
24
25 (2) Portehault, D.; Delacroix, S.; Gouget, G.; Grosjean, R.; Chan-Chang, T.-H.-C.
26
27
28 Beyond the Compositional Threshold of Nanoparticle-Based Materials. *Acc. Chem.*
29
30
31
32 *Res.* **2018**, *51*, 930–939. <https://doi.org/10.1021/acs.accounts.7b00429>.
33
34
35
36 (3) Carenco, S.; Portehault, D.; Boissière, C.; Mézailles, N.; Sanchez, C. Nanoscaled
37
38
39 Metal Borides and Phosphides: Recent Developments and Perspectives. *Chem.*
40
41
42
43 *Rev.* **2013**, *113*, 7981–8065. <https://doi.org/10.1021/cr400020d>.
44
45
46 (4) Thi N’Goc, H. Le; Mouafo, L. D. N.; Etrillard, C.; Torres-Pardo, A.; Dayen, J.-F.;
47
48
49
50 Rano, S.; Rousse, G.; Laberty-Robert, C.; Calbet, J. G.; Drillon, M.; et al. Surface-
51
52
53 Driven Magnetotransport in Perovskite Nanocrystals. *Adv. Mater.* **2017**, *29*,
54
55
56
57
58
59
60

- 1
2
3
4 1604745. <https://doi.org/10.1002/adma.201604745>.
5
6
7 (5) Li, L.; Deng, J.; Chen, J.; Xing, X. Topochemical Molten Salt Synthesis for
8
9
10 Functional Perovskite Compounds. *Chem. Sci.* **2016**, *7* (2), 855–865.
11
12
13
14 <https://doi.org/10.1039/c5sc03521j>.
15
16
17 (6) Liu, H.; Hu, C.; Wang, Z. L. Composite-Hydroxide-Mediated Approach for the
18
19
20 Synthesis of Nanostructures of Complex Functional-Oxides. *Nano Lett.* **2006**, *6*(7),
21
22
23
24 1535–1540. <https://doi.org/10.1021/nl061253e>.
25
26
27 (7) Portehault, D.; Devi, S.; Beaunier, P.; Gervais, C.; Giordano, C.; Sanchez, C.;
28
29
30
31 Antonietti, M. A General Solution Route toward Metal Boride Nanocrystals. *Angew.*
32
33
34
35 *Chem. Int. Ed.* **2011**, *50*(14), 3262–3265. <https://doi.org/10.1002/anie.201006810>.
36
37
38 (8) Gouget, G.; Beaunier, P.; Portehault, D.; Sanchez, C. New Route toward
39
40
41
42 Nanosized Crystalline Metal Borides with Tunable Stoichiometry and Variable
43
44
45
46 Morphologies. *Faraday Discuss.* **2016**, *191*, 511–525.
47
48
49 (9) Gouget, G.; Debecker, D. P.; Kim, A.; Olivieri, G.; Gallet, J.-J.; Bournel, F.; Thomas,
50
51
52
53 C.; Ersen, O.; Moldovan, S.; Sanchez, C.; et al. In Situ Solid-Gas Reactivity of
54
55
56
57 Nanoscaled Metal Borides from Molten Salt Synthesis. *Inorg. Chem.* **2017**, *56*,
58
59
60

1
2
3
4 9225–9234.
5
6

- 7 (10) Liu, X.; Antonietti, M.; Giordano, C. Manipulation of Phase and Microstructure at
8
9
10 Nanoscale for SiC in Molten Salt Synthesis. *Chem. Mater.* **2013**, *25* (10), 2021–
11
12
13 2027. <https://doi.org/10.1021/cm303727g>.
14
15
16
17 (11) Liu, X.; Giordano, C.; Antonietti, M. A Molten-Salt Route for Synthesis of Si and Ge
18
19
20 Nanoparticles: Chemical Reduction of Oxides by Electrons Solvated in Salt Melt. *J.*
21
22
23 *Mater. Chem.* **2012**, *22* (12), 5454. <https://doi.org/10.1039/c2jm15453f>.
24
25
26
27 (12) Konstantakou, M.; Stergiopoulos, T. A Critical Review on Tin Halide Perovskite
28
29
30 Solar Cells. *J. Mater. Chem. A* **2017**, *5* (23), 11518–11549.
31
32
33
34
35 <https://doi.org/10.1039/C7TA00929A>.
36
37
38 (13) Hashim, S. S.; Somalu, M. R.; Loh, K. S.; Liu, S.; Zhou, W.; Sunarso, J. Perovskite-
39
40
41 Based Proton Conducting Membranes for Hydrogen Separation: A Review. *Int. J.*
42
43
44 *Hydrogen Energy* **2018**, *43* (32), 15281–15305.
45
46
47
48
49 <https://doi.org/10.1016/j.ijhydene.2018.06.045>.
50
51
52 (14) Sunarso, J.; Hashim, S. S.; Zhu, N.; Zhou, W. Perovskite Oxides Applications in
53
54
55 High Temperature Oxygen Separation, Solid Oxide Fuel Cell and Membrane
56
57
58
59
60

- 1
2
3
4 Reactor: A Review. *Prog. Energy Combust. Sci.* **2017**, *61*, 57–77.
5
6
7 <https://doi.org/10.1016/j.pecs.2017.03.003>.
8
9
10 (15) Ansari, M. I. H.; Qurashi, A.; Nazeeruddin, M. K. Frontiers, Opportunities, and
11
12 Challenges in Perovskite Solar Cells: A Critical Review. *J. Photochem. Photobiol.*
13
14 *C Photochem. Rev.* **2018**, *35*, 1–24.
15
16
17 <https://doi.org/10.1016/j.jphotochemrev.2017.11.002>.
18
19
20
21 (16) Lobanov, M. V.; Li, S.; Greenblatt, M. Structural, Magnetic, and Transport
22
23 Properties of the Two Electron-Doped Ruddlesden–Popper Manganites Ca_{3-x}Th
24
25 $x\text{Mn}_2\text{O}_7$. *Chem. Mater.* **2003**, *15* (6), 1302–1308.
26
27
28
29
30
31 <https://doi.org/10.1021/cm020470n>.
32
33
34
35 (17) Demont, A.; Hébert, S.; Pelloquin, D.; Maignan, A. The $\text{Sr}_{2.75}\text{Ce}_{0.25}\text{Co}_2\text{O}_{7-\delta}$
36
37 Oxide, N=2 Member of the Ruddlesden–Popper Series: Structural and Magnetic
38
39 Evolution Depending on Oxygen Stoichiometry. *J. Solid State Chem.* **2008**, *181* (6),
40
41 1314–1320. <https://doi.org/10.1016/j.jssc.2008.02.023>.
42
43
44
45 (18) Zhu, J.; Thomas, A. Perovskite-Type Mixed Oxides as Catalytic Material for NO
46
47 Removal. *Appl. Catal. B Environ.* **2009**, *92* (3–4), 225–233.
48
49
50
51
52
53
54
55
56
57
58
59
60

1
2
3
4 <https://doi.org/10.1016/j.apcatb.2009.08.008>.

- 5
6
7 (19) Suntivich, J.; Gasteiger, H. a; Yabuuchi, N.; Nakanishi, H.; Goodenough, J. B.;
8
9
10 Shao-Horn, Y. Design Principles for Oxygen-Reduction Activity on Perovskite
11
12
13
14 Oxide Catalysts for Fuel Cells and Metal-Air Batteries. *Nat. Chem.* **2011**, *3*(7), 546–
15
16
17 550. <https://doi.org/10.1038/nchem.1069>.
18
19
20
21 (20) Yu, J.; Sunarso, J.; Zhu, Y.; Xu, X.; Ran, R.; Zhou, W.; Shao, Z. Activity and Stability
22
23
24 of Ruddlesden-Popper-Type $\text{La}_{n+1}\text{Ni}_n\text{O}_{3n+1}$ ($n = 1, 2, 3, \text{ and } \infty$) Electrocatalysts
25
26
27 for Oxygen Reduction and Evolution Reactions in Alkaline Media. *Chem. - A Eur.*
28
29
30
31 *J.* **2016**, *22*, 1–10. <https://doi.org/10.1002/chem.201504279>.
32
33
34
35 (21) Zhang, J.; Zhao, Y.; Zhao, X.; Liu, Z.; Chen, W. Porous Perovskite LaNiO_3
36
37
38 Nanocubes as Cathode Catalysts for Li-O₂ Batteries with Low Charge Potential.
39
40
41
42 *Sci. Rep.* **2015**, *4* (1), 6005. <https://doi.org/10.1038/srep06005>.
43
44
45
46 (22) Wei, Z.; Cui, Y.; Huang, K.; Ouyang, J.; Wu, J.; Baker, A. P.; Zhang, X. Fabrication
47
48
49 of La_2NiO_4 Nanoparticles as an Efficient Bifunctional Cathode Catalyst for
50
51
52 Rechargeable Lithium–Oxygen Batteries. *RSC Adv.* **2016**, *6* (21), 17430–17437.
53
54
55
56 <https://doi.org/10.1039/C5RA23053E>.
57
58
59
60

- 1
2
3
4 (23) Pikalova, E. Y.; Bogdanovich, N. M.; Kolchugin, A. A.; Osinkin, D. A.; Bronin, D. I.
5
6
7 Electrical and Electrochemical Properties of La₂NiO_{4+δ}-Based Cathodes in
8
9
10 Contact with Ce_{0.8}Sm_{0.2}O_{2-δ} Electrolyte. *Procedia Eng.* **2014**, *98*, 105–110.
11
12
13
14 <https://doi.org/10.1016/j.proeng.2014.12.495>.
15
16
17 (24) Woolley, R. J.; Skinner, S. J. Functionally Graded Composite La₂NiO_{4+δ} and La
18
19
20 4 Ni₃O_{10-δ} Solid Oxide Fuel Cell Cathodes. *Solid State Ionics* **2014**, *255*, 1–5.
21
22
23
24 <https://doi.org/10.1016/j.ssi.2013.11.041>.
25
26
27 (25) BOEHM, E.; BASSAT, J.; DORDOR, P.; MAUVY, F.; GRENIER, J.; STEVENS, P.
28
29
30
31 Oxygen Diffusion and Transport Properties in Non-Stoichiometric LnNiO Oxides.
32
33
34
35 *Solid State Ionics* **2005**, *176* (37–38), 2717–2725.
36
37
38
39 <https://doi.org/10.1016/j.ssi.2005.06.033>.
40
41
42 (26) Gonell, F.; Sanchez-Sanchez, C. M.; Vivier, V.; Méthivier, C.; Laberty-Robert, C.;
43
44
45 Portehault, D. Structure-Activity Relationship in Manganese Perovskite Oxide
46
47
48
49 Nanocrystals from Molten Salts for Efficient Oxygen Reduction Reaction
50
51
52
53 Electrocatalysis. *Chem. Mater.* **2020**, *10.1021/ac*.
54
55
56
57 <https://doi.org/10.1021/acs.chemmater.0c00681>.
58
59
60

- 1
2
3
4 (27) Gonell, F.; Alem, N.; Dunne, P.; Crochet, G.; Beaunier, P.; Méthivier, C.; Montero,
5
6
7 D.; Laberty-Robert, C.; Doudin, B.; Portehault, D. Versatile Molten Salt Synthesis
8
9
10 of Manganite Perovskite Oxide Nanocrystals and Their Magnetic Properties.
11
12
13 *ChemNanoMat* **2019**, *5* (3), 358–363. <https://doi.org/10.1002/cnma.201800632>.
14
15
16
17 (28) Al Raihani, H.; Durand, B.; Chassagneux, F.; Kerridge, D. H.; Inman, D. Zirconia
18
19
20 Formation by Reaction of Zirconium Sulfate in Molten Alkali-Metal Nitrates or
21
22
23 Nitrites. *J. Mater. Chem.* **1994**, *4* (8), 1331. <https://doi.org/10.1039/jm9940401331>.
24
25
26
27 (29) Du, Y.; Inman, D. Reactions of $Zr(SO_4)_2$ in Molten Nitrite and Nitrate Systems. *J.*
28
29
30 *Mater. Chem.* **1995**, *5* (11), 1927. <https://doi.org/10.1039/jm9950501927>.
31
32
33
34 (30) Du, Y.; Inman, D. The Acidic/Basic Effects on Preparation of Zirconia Powders from
35
36
37 Molten Salts. *J. Mater. Sci.* **1996**, *31* (13), 5505–5511.
38
39
40
41 <https://doi.org/10.1007/BF00360735>.
42
43
44
45 (31) Du, Y.; Inman, D. Synthesis of MgO Powders from Molten Salts. *J. Mater. Sci.* **1997**,
46
47
48 *2*, 2373–2379.
49
50
51
52 (32) Jolivet, J.-P. *Metal Oxide Chemistry and Synthesis: From Solution to Solid State*;
53
54
55 Wiley: Chichester, 2000.
56
57
58
59
60

- 1
2
3
4 (33) Deshmukh, R.; Niederberger, M. Mechanistic Aspects in the Formation, Growth and
5
6
7 Surface Functionalization of Metal Oxide Nanoparticles in Organic Solvents. *Chem.*
8
9
10 - *A Eur. J.* **2017**. <https://doi.org/10.1002/chem.201605957>.
11
12
13
14 (34) Afanasiev, P.; Geantet, C. Synthesis of Solid Materials in Molten Nitrates. *Coord.*
15
16
17 *Chem. Rev.* **1998**, *178–180* (PART 2), 1725–1752. <https://doi.org/10.1016/s0010->
18
19
20
21 8545(98)00154-4.
22
23
24 (35) Cui, Z.; Wang, S.; Zhang, Y.; Cao, M. Engineering Hybrid between Nickel Oxide
25
26
27 and Nickel Cobaltate to Achieve Exceptionally High Activity for Oxygen Reduction
28
29
30
31 Reaction. *J. Power Sources* **2014**, *272*, 808–815.
32
33
34
35 <https://doi.org/10.1016/j.jpowsour.2014.08.097>.
36
37
38 (36) Stoerzinger, K. a.; Lü, W.; Li, C.; Ariando; Venkatesan, T.; Shao-Horn, Y. Highly
39
40
41 Active Epitaxial La(1-x)SrxMnO3 Surfaces for the Oxygen Reduction Reaction:
42
43
44 Role of Charge Transfer. *J. Phys. Chem. Lett.* **2015**, *6*, 1435–1440.
45
46
47
48
49 <https://doi.org/10.1021/acs.jpcllett.5b00439>.
50
51
52 (37) Retuerto, M.; Pereira, A. G.; Pérez-Alonso, F. J.; Peña, M. A.; Fierro, J. L. G.;
53
54
55
56 Alonso, J. A.; Fernández-Díaz, M. T.; Pascual, L.; Rojas, S. Structural Effects of
57
58
59
60

1
2
3
4 LaNiO₃ as Electrocatalyst for the Oxygen Reduction Reaction. *Appl. Catal. B*
5
6
7 *Environ.* **2017**, *203*, 363–371. <https://doi.org/10.1016/j.apcatb.2016.10.016>.
8
9

10 (38) Ji, Q.; Bi, L.; Zhang, J.; Cao, H.; Zhao, X. S. The Role of Oxygen Vacancies of ABO
11
12
13
14 3 Perovskite Oxides in the Oxygen Reduction Reaction. *Energy Environ. Sci.* **2020**,
15
16
17 *13* (5), 1408–1428. <https://doi.org/10.1039/D0EE00092B>.
18
19
20
21
22
23
24
25
26
27
28
29
30
31
32
33
34
35
36
37
38
39
40
41
42
43
44
45
46
47
48
49
50
51
52
53
54
55
56
57
58
59
60

Table of contents

